Atomic Structure of Phosphorylated Nanocellulose Revealed by Dynamic Nuclear Polarization-Enhanced Solid-State NMR

Tomohito Yagita, Subhradip Paul, Wassilios Papawassiliou, Akane Sakiyama, Yuka Tomita, Tsuguyuki Saito, Sabine Hediger, Gaël de Paëpe, Shuji Fujisawa

JACS
JOURNAL OF THE AMERICAN CHEMICAL SOCIETY
pubs.acs.org/JACS

Article

Atomic Structure of Phosphorylated Nanocellulose Revealed by Dynamic Nuclear Polarization-Enhanced Solid-State NMR

Tomohito Yagita, Subhradip Paul, Wassilios Papawassiliou, Akane Sakiyama, Yuka Tomita, Tsuguyuki Saito, Sabine Hediger, Gaël De Paëpe,* and Shuji Fujisawa*

Cite This: J. Am. Chem. Soc. 2026, 148, 4237−4249

Read Online

ACCESS | Metrics & More | Article Recommendations | Supporting Information

ABSTRACT: Atomic-level details of nanocellulose structure, particularly at its surface, remain difficult to resolve and are therefore poorly understood. Here we apply dynamic nuclear polarization (DNP)-enhanced solid-state NMR to directly probe the surface chemistry of phosphorylated cellulose nanofibers. Multidimensional $^{13}C-^{13}C$ and $^{31}P-^{13}C$ correlation experiments reveal both mono- and diphosphate substitution, with C2 and C6 identified as the preferred sites. Quantitative multiCP analysis establishes the degree of phosphorylation and the conformational distribution of surface phosphate groups, while $^{31}P-^{31}P$ correlations reveal their corresponding spatial distribution. The site-specific phosphorylation derived from DNP-NMR data was used to construct a CNF model for molecular dynamics (MD) simulations, which reproduce the fibril twisting observed by AFM and yield $^{31}P-^{31}P$ radial distribution functions consistent with the DNP-NMR data. In addition, the MD-derived C6 phosphorylated and nonphosphorylated conformational distribution both within the fibril core and at its surface is in agreement with the DNP-NMR data. To rationalize the preferred conformations of phosphorylated C6 groups observed in both NMR experiments and MD simulations, DFT calculations were carried out and show that these conformations are governed by facet-dependent hydrogen-bond formation at the nanocellulose surface.

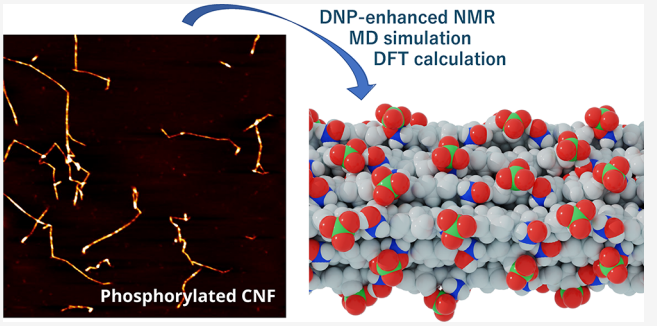

1. INTRODUCTION

Nanocellulose, which is derived from natural resources such as wood and plants, has attracted significant attention because of its excellent physical and chemical properties, offering sustainable benefits in various fields such as materials science, biotechnology, cosmetics, and medicine.[1−3] Nanocellulose production involves the disintegration of tightly packed cellulose fibrils present in cell walls into nanosized units. This process requires significant mechanical energy to overcome the inherent strong attractive forces between fibrils. To increase the energy efficiency of the disintegration process, chemical pretreatment is typically employed; this results in the introduction of functional groups, such as phosphates, carboxylates, sulfates and amine groups, onto the fibril surface,[4] which facilitates their separation. Owing to the variety of chemical pretreatments available, nanocellulose has a wide range of shapes and surface chemistries, enabling material performance, such as chemical, mechanical, and rheological properties, to be tailored. To optimize their use in materials applications, a fundamental understanding of the atomic-level morphology and surface chemistry of nanocellulose is critical.

Historically, microscopic techniques such as transmission electron microscopy (TEM)[5−8] and atomic force microscopy (AFM)[6−10] have been extensively used to observe the morphology of nanocelluloses. Additionally, X-ray scattering has been employed to analyze their crystalline structure and cross-sectional sizes.[5,11−15] With the advancement of these techniques, the understanding of the morphology of nanocellulose has markedly progressed, and the fundamental cellulose fibril derived from wood has recently been described as being composed of 18 cellulose chains.[16,17] However, while the morphology of nanocelluloses can be observed in detail, these techniques lack the resolution needed at the atomic scale to identify chemical surface modifications. This limitation has hindered a thorough spatial understanding of the chemical composition of nanocellulose surfaces. Elemental analysis and energy-dispersive X-ray spectroscopy are also used for the chemical analysis of cellulose, providing quantitative atomic information from spectral data, but these methods do not directly capture the structural details of nanocellulose surfaces.[18]

Received: September 29, 2025
Revised: January 5, 2026
Accepted: January 9, 2026
Published: January 23, 2026

https://doi.org/10.1021/jacs.5c17152
J. Am. Chem. Soc. 2026, 148, 4237−4249

In contrast, solid-state ^{13}C cross-polarization magic angle spinning nuclear magnetic resonance (CPMAS NMR) provides information about the local atomic environment, enabling detailed characterization of molecular structures. Since the pioneering solid-state NMR studies by Atalla et al.[19] and Earl and VanderHart[20] in 1980, solid-state NMR has been widely used to understand the polymorphs[21−25] and crystallinities[26−29] of cellulose. In addition, NMR has the capability to differentiate crystalline and amorphous contributions, as well as to detect conformational arrangements and cross-sectional size of cellulose crystallites,[10−12,30,31] offering critical information about the surface chemistry of nanocellulose. However, a major challenge associated with ^{13}C CPMAS NMR is its limited sensitivity, related to the low natural abundance of ^{13}C (~1.1%),[18,32] which severely hinders the ability to obtain detailed atomic information on samples at natural isotopic abundance (NA).

This long-standing limitation has been effectively addressed with the advent of Dynamic nuclear polarization (DNP)-enhanced NMR, which has emerged as a transformative approach for overcoming intrinsic sensitivity barriers.[33−37] In DNP, polarization is transferred from unpaired electrons to nearby nuclei, resulting in signal enhancements of several orders of magnitude.[36] A key milestone was achieved in 2012 by Takahashi et al. with the report that DNP could be used to record $^{13}C-^{13}C$ correlation spectra of microcrystalline cellulose at NA within an hour.[38] Importantly, this work also established that dipolar-based polarization transfer at NA can be exploited to probe long-distance polarization transfer (owing to the absence of dipolar truncation).[39] Building on this, Kumar et al. investigated the surface chemical structure of surface-grafted nanocellulose by DNP-enhanced NMR and succeeded in detecting the weak peak signals of grafting moieties, which accounted for only 1% of the cellulose chains.[40] DNP-enhanced NMR has also been applied to other surface-modified cellulose or lignocellulosic materials,[41−48] providing critical information on interfaces and surfaces.

In this contribution, we combined DNP-enhanced NMR and computational methods, including molecular dynamics (MD) simulations and density functional theory (DFT) calculations, to probe the chemical structure of the nanocellulose surface at atomic resolution. Our results provide, for the first time, a precise understanding of the chemical surface topology of surface-phosphorylated-cellulose nanofibers (P-CNFs), including the substitution positions, spatial distribution, and conformation of the surface molecules.

2. METHODS

2.1. Materials

Phosphorylated pulp (total charge: 2.27 mmol g^{-1}) was kindly provided by Oji Holdings Corporation. Phosphorylated pulp was prepared according to previously reported procedures.[49,50] Briefly, once-dried softwood bleached kraft pulp sheets were impregnated with an aqueous mixed solution comprising phosphoric acid and urea. The impregnated pulp sheets were then phosphorylated by heating in an oven. After the reaction, the pulp was thoroughly washed with deionized water to remove excess reagents. A sodium hydroxide solution was subsequently added to the pulp suspension to neutralize the phosphate groups with sodium ions, followed by repeated washing to remove any residual chemicals. *tert*-Butyl alcohol, D_2O, and AMUPol were purchased from Wako Chemical Co., Ltd., Sigma−Aldrich, and Cortecnet, respectively, and were used as received.

2.2. Potentiometric Titration

To determine the amount of dissociated protons within the phosphate groups, potentiometric titration of the protonated phosphorylated pulp was performed using 0.1 M NaOH aqueous solution. In accordance with previously reported procedures, the amounts of the first and second dissociated protons were determined on the basis of the amount of NaOH needed for the first and second equivalent points, respectively.[49]

2.3. Preparation of P-CNFs

Phosphorylated pulp was suspended in distilled water with a pulp concentration of 0.3% w/w and disintegrated to produce nanofibrillated P-CNF by operating a mechanical homogenizer (Physcotron NS-56, Nihonseiki Kaisha Ltd., Japan) at 7,500 rpm for 2 min, followed by ultrasonication (US-300T, Nihonseiki Kaisha Ltd., Japan) at 19.5 kHz for 16 min. Undisintegrated fractions were removed by centrifugation at 8,300 rpm for 15 min. The resulting P-CNF aqueous dispersion was stored at 4 °C.

2.4. AFM Experiments

The P-CNF aqueous dispersion was diluted to 0.0002% w/w, and 10 μL of the diluted dispersion was dropped on a smooth mica surface immediately after cleavage, which was then dried under reduced pressure by using a diaphragm pump for 15 min. AFM observations were conducted using a MultiMode 8 microscope (Bruker, USA) equipped with a NanoScope V controller and a ScanAsyst-Air probe in peak-force tapping mode. The scan size was 2 × 2 μm^2, and the pixel resolution was 1024 pixels per line. AFM image processing and AFM height analyses were performed using NanoScope Analysis software (version 1.7; Bruker, USA).

2.5. Sample Preparation for DNP-Enhanced Solid-State NMR

The P-CNF aqueous dispersion was freeze-dried after approximately 30% w/w *tert*-butyl alcohol with respect to its water content was added to suppress dry agglomeration. Fifty-six milligrams of freeze-dried P-CNF was impregnated with 80 μL of DNP matrix solution composed of 10 mM AMUPol[51] radical in D_2O. This impregnated sample was ground with a pestle and then packed into a 3.2 mm zirconia rotor.

2.6. DNP-Enhanced Solid-State NMR Experiments

All the experiments were performed on a Bruker Avance III 400 MHz (^1H resonance) DNP-NMR spectrometer equipped with a 263 GHz gyrotron for microwave irradiation at 105 K. Chemical shift referencing was performed indirectly at room temperature using the CH signal of adamantane for ^{13}C at 37.8 ppm and that of hydroxyapatite for ^{31}P at 2.8 ppm.[52,53] It is important to note that ^{13}C and ^{31}P chemical shifts measured under low-temperature DNP conditions can differ from room-temperature values in a site-dependent manner. However, this does not change the overall conclusions of this study. The pulse-sequence-related parameters for all the solid-state NMR experiments are summarized in Tables S2 and S3. All the data were recorded and processed with Bruker Topspin version 3.6.3 and plotted using nmrglue[54] and Python.

To determine the average distance between phosphorus atoms on the surface of P-CNFs, the S_3 experimental buildup curves were fitted using a library of simulated buildup curves generated with SIMPSON[55] for dipolar couplings ranging from 50 to 350 Hz for monophosphate groups and from 700 to 1500 Hz for diphosphate groups in 1 Hz steps. The root-mean-square deviation (RMSD) between the experimental curve and each simulated buildup curve was then minimized by adjusting only the scaling factor A and the decay time constant τ_{decay} of the simulated curve according to the following equation:

$$RMSD(A, \tau_{decay}) = \sqrt{\frac{1}{N}\sum_{\tau_{mix}}\left[I_{exp}(\tau_{mix}) - A\left(I_{sim}(\tau_{mix}, d)\cdot\exp\left[-\frac{\tau_{mix}}{\tau_{decay}}\right]\right)\right]^2}$$

https://doi.org/10.1021/jacs.5c17152
J. Am. Chem. Soc. 2026, 148, 4237−4249

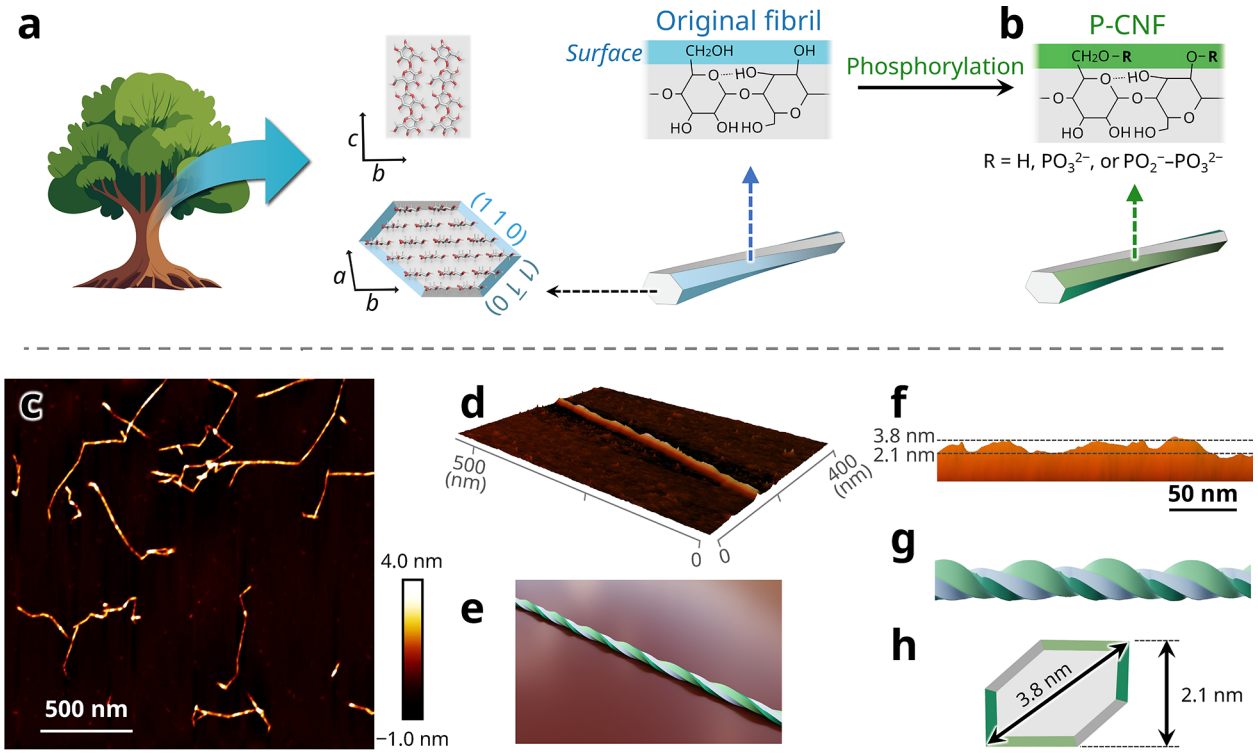

Figure 1. Schematic illustration of the preparation of P-CNFs from wood and their morphology; (a) CNF structural model containing 18 cellulose chains with a 234432 arrangement; (b) expected surface modification upon phosphorylation. The C2 and C6 hydroxy groups exposed on the (1 1 0) and (1 $\bar{1}$ 0) faces (light and dark blue, respectively) are expected to be selectively phosphorylated (light and dark green, respectively); (c) AFM image of P-CNFs; (d) side-view AFM image and (e) 3D image of a single P-CNF; corresponding (f) side-view and (g) 3D image of a P-CNF model showing (h) the cross section of the 18-chain P-CNF model.

where $I_{exp}(\tau_{mix})$ and $I_{sim}(\tau_{mix}, d)$ are the experimental and simulated peak intensities, respectively, as a function of the mixing time τ_{mix} and the dipolar coupling d for the simulated data and N is the number of experimental points in the buildup curve. The experimental peak intensities were extracted from the integrated areas of the individual peaks.

2.7. MD Simulations

The P-CNF model, consisting of 18 chains[10,16,56] with 80 glycosyl residues, was built on the basis of the experimental crystal structure of the I_β allomorph.[57] The total amount of phosphoester groups was set to ~1.15 mmol g^{-1} (total charge: 2.29 mol g^{-1}). The molar ratio of phosphorylation between the surface C2 and C6 positions was 25:75, which was based on the experimental results from 2D $^{31}P-^{13}C$ TEDOR. To model the CNFs containing sodium phosphate groups, sodium ions were introduced into the system to counterbalance the phosphate groups. All-atom molecular dynamics simulations were performed using GROMACS version 2021.1 and CHARMM C36[58,59] as the force field. The initial structure was solvated with water molecules in a periodic box with dimensions of 12 × 14 × 52 nm^3. Electrostatic interactions and short-range van der Waals interactions were cut off above 1.0 nm. The particle mesh Ewald (PME) method was applied to include long-range electrostatic interactions. The system was subjected to 1000 steps for steepest descent minimization, and a 1000 kcal mol^{-1} nm^{-2} constraint was applied only to the heavy atoms of the CNFs. Afterward, the system was relaxed with 1000 steps of steepest descent minimization without restraint. Afterward, the temperature of the system was increased gradually to 300 K with the NVT ensemble for 1 ns and subsequently with the NPT ensemble for 1 ns with position restraint on the heavy atoms (1000 kcal mol^{-1} nm^{-2}) of the CNF. The Berendsen weak coupling algorithm was used to maintain a constant temperature and pressure.[60] Afterward, an MD production run was carried out for 15 ns by using the Parrinello–Rahman barostat without any position restraint.[61] The simulations were performed with the LINCS constraint, where the integration time step was 2 fs. PyMol software (https://pymol.org/2/) was used to generate structural visualizations.

2.8. DFT Calculations

Structural relaxation of the P-CNF surface models was performed using the Quantum ESPRESSO package.[62] Initially, the system underwent a primary relaxation phase by employing the damping method, which was aimed at reducing initial stresses and bringing the structure closer to its equilibrium state. This was subsequently followed by a secondary, more refined phase of relaxation using the Broyden–Fletcher–Goldfarb–Shanno (BFGS) algorithm. The simulations incorporated van der Waals corrections via the DFT-D3 method.[63] The Perdew–Burke–Ernzerhof (PBE) functional was used for the exchange–correlation energy.[64] The convergence of the self-consistent field (SCF) calculations was meticulously monitored, with a convergence threshold of $1.0e^{-7}$, to ensure that the electronic structure precisely reached its ground state. A self-consistent field (SCF) calculation was executed to obtain the converged ground-state electronic structure of the system. The settings included the application of DFT-D3 van der Waals corrections and the use of the PBE exchange-correlation functional. The kinetic energy cutoff for wave functions was set to 60 Ry, and the kinetic energy cutoff for charge density was 720 Ry. The k-point sampling was set to a 2 × 2 × 2 Monkhorst–Pack grid.[64]

3. RESULTS AND DISCUSSION

3.1. Morphology of Phosphorylated Cellulose Nanofibers (P-CNFs)

The schematics of wood-derived P-CNF preparation and its morphology are shown in Figure 1. Native crystalline cellulose fibrils are predominantly composed of a monoclinic unit cell, known as cellulose I_β,[65] in which hydroxy groups are densely exposed on the (1 1 0) and (1 $\bar{1}$ 0) faces. Upon phosphorylation, the hydroxy groups on the fibril surfaces (Figure 1a) are

https://doi.org/10.1021/jacs.5c17152
J. Am. Chem. Soc. 2026, 148, 4237–4249

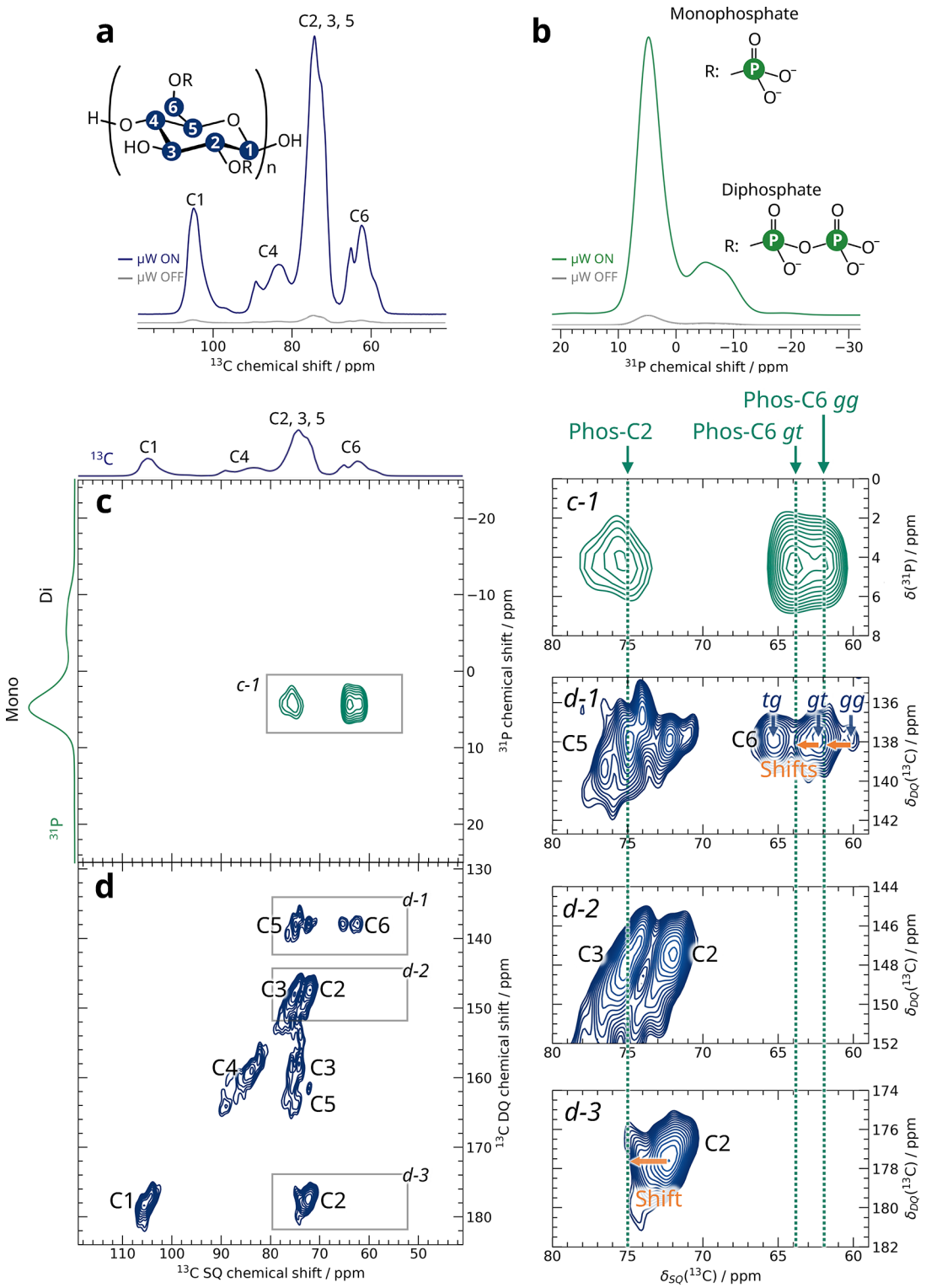

Figure 2. DNP-enhanced NMR spectra of P-CNFs; DNP-enhanced (a) ^{13}C and (b) ^{31}P CPMAS NMR spectra of P-CNFs with (blue and green spectra, respectively) and without (gray spectra) microwave (μw) irradiation suitable for DNP. DNP-enhanced 2D (c) $^{31}P-^{13}C$ TEDOR and (d) double-quantum (DQ)−single-quantum (SQ) $^{13}C-^{13}C$ INADEQUATE spectra of P-CNFs, with enlarged regions shown in c-1 and d-1 to d-3. Spectra are displayed with identical ^{13}C chemical shift axes to allow direct comparison. The assignment is given in the figure. Carbon chemical shifts of phosphorylated C2 (Phos-C2) and phosphorylated C6 with *gt* (Phos-C6*gt*) and *gg* (Phos-C6*gg*) conformations are indicated by the three vertical green dashed lines. Downfield shifts in ^{13}C chemical shifts upon phosphorylation are indicated by orange arrows.

derivatized to phosphoester groups (Figure 1b).[50,66] The anionic phosphate groups introduced on the surface make it possible to isolate and disperse individual cellulose fibrils in water by generating repulsive forces between the fibrils, such as osmotic pressure.

The AFM image of the P-CNFs, which are individually dispersed on the mica substrate, is shown in Figure 1c. Each

https://doi.org/10.1021/jacs.5c17152
J. Am. Chem. Soc. 2026, 148, 4237−4249

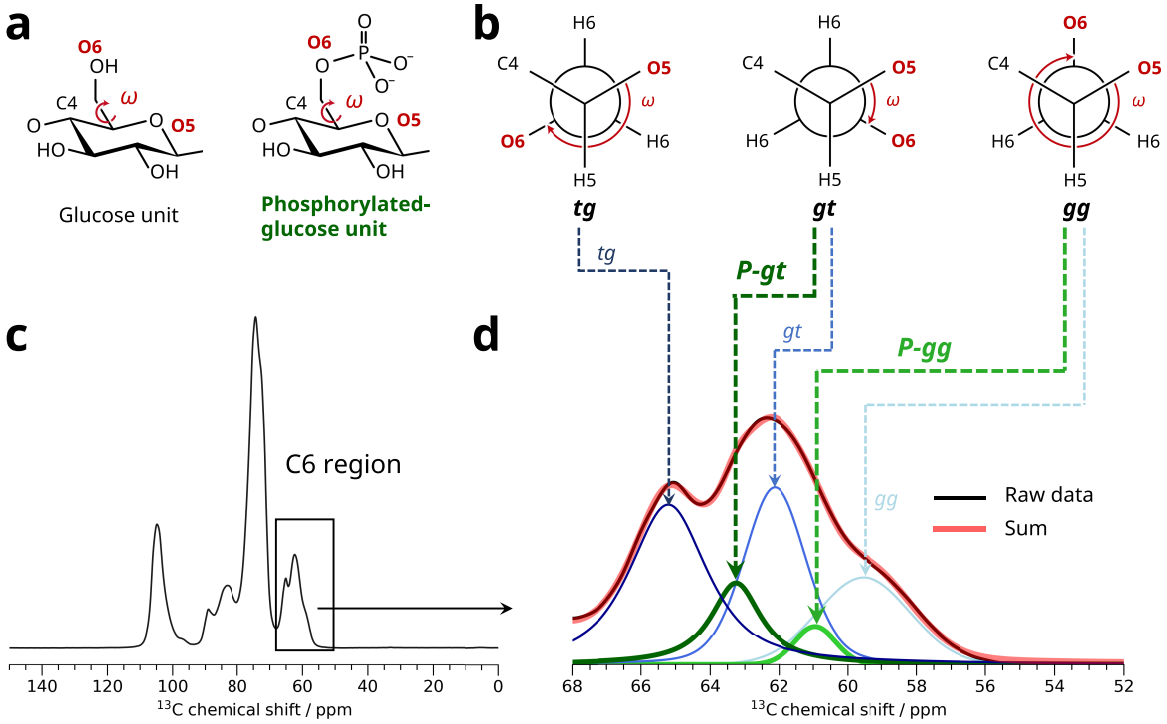

Figure 3. Chemical shifts and conformational analysis of the C6 region of P-CNFs; (a) Native and phosphorylated glucose units and (b) three distinct rotamers in relation to the O5−C5−C6−O6 dihedral angle (ω). These rotamers are designated as *gauche−gauche* (*gg*), *gauche−trans* (*gt*), and trans-*gauche* (*tg*). The designation "*gauche*" or "*trans*" in the first descriptor refers to the torsional relationship between the O5 and O6 atoms, depending on the O5−C5−C6−O6 dihedral angle ω ($\omega = \pm 60°$ for *g* and 180° for *t*). Similarly, the second descriptor indicates the torsional relationship between the C4 and O6 atoms, which is related to the C4−C5−C6−O6 dihedral angle. Similarly, the ω *values of the gt, tg,* and *gg* conformers are 60 ± 60°, 180 ± 60°, and 300 ± 60°, respectively. (c) DNP-enhanced ^{13}C multiCP spectrum of P-CNF. (d) C6 region of the spectrum given in (c) (in black) and its deconvolution using 5 components centered at the chemical shift positions found in the 2D ^{31}P−^{13}C TEDOR and ^{13}C−^{13}C INADEQUATE spectra. The assignments of the different contributions are given in the figure, with those of the three rotamers found in native C6 shown in dark blue, medium blue, and light blue and the two rotamers corresponding to phosphorylated C6 shown in dark green and light green. The red spectrum is the sum of the five contributions.

individual P-CNF exhibits a twisted morphology along the fibril axis (Figure 1e and Figure S1), which agrees with previous AFM[6−9,67−69] and TEM[6−8] studies. In our case, the AFM height image of P-CNF shows a periodicity pitch of approximately 50 nm (Figure 1f), which is in good agreement with results previously reported for CNFs prepared from wood.[67,69] The maximum and minimum heights of P-CNF are ∼3.8 and ∼2.1 nm, respectively (Figure 1f). These values are consistent with those predicted for the cross-section of the 18-chain CNF model (Figure 1h),[10,16,17,56] highlighting consistency with the expected overall fibril structure (Figure 1e, g).

3.2. Investigation of the Surface Chemistry and C6 Conformation of P-CNFs by DNP-Enhanced NMR

The capacity of MAS-DNP to significantly increase the sensitivity of ^{13}C and ^{31}P NMR experiments is demonstrated in Figures 2a and b, which compare the 1D ^{13}C and ^{31}P CPMAS spectra of P-CNF, respectively, acquired at 105 K with and without microwave irradiation (μw). The significant increase in intensity obtained with DNP is acknowledged by the sizable ^{1}H enhancement factor $\varepsilon_{on/off}$ (the ratio of the signal intensity with and without μw) of ∼30 for the ^{13}C/^{31}P CPMAS experiments. Deconvolution of the ^{31}P CPMAS spectrum revealed a monophosphate-to-diphosphate ratio of approximately 84:16 (Figure S2).

Owing to the improvement in sensitivity provided by DNP, 2D NMR spectra were successfully obtained for P-CNFs at natural isotopic abundance. The 2D ^{31}P−^{13}C TEDOR[70,71] and ^{13}C−^{13}C INADEQUATE[72] spectra are shown in Figure 2c and d, respectively. The ^{13}C−^{13}C INADEQUATE experiment yielded the expected strong cross peaks correlating chemically bonded carbon atoms within the glucose unit. In addition, the fine structure of the cross-peak patterns reveals detailed chemical and conformational information on the various carbon atoms in P-CNFs. The ^{31}P−^{13}C TEDOR spectrum was acquired with a short mixing time of 1 ms, in order to favor polarization transfer over short distances. The correlation peaks observed in this spectrum indicate the close spatial proximity of carbon atoms to phosphorus atoms, suggesting covalent bonds between the CNFs and phosphate groups and, therefore, the successful phosphorylation of CNFs.

In the INADEQUATE spectrum, the C6 hydroxymethyl group appears to present three main chemical shifts (Figure 2d-1). This finding is fully consistent with the literature reporting the presence of three conformers,[73−75] corresponding to three distinct rotamers, designated *gauche−gauche* (*gg*), *gauche−trans* (*gt*), and trans-*gauche* (*tg*), depending on the O5−C5−C6-O6 dihedral angle (ω) (Figure 3a, b). Lowering the contour levels of the C5−C6 cross-peaks (Figure 2d-1) reveals additional contributions, which can be also observed from the ^{31}P−^{13}C TEDOR experiment (Figure 2c-1), and thus correspond to phosphorylated C6. Interestingly, the TEDOR spectrum shows mainly two contributions, at 63.4 and 61.6 ppm, which are consistent with the presence of *gt* and *gg* conformations, since the C6 chemical shifts shift downfield upon phosphorylation as a

https://doi.org/10.1021/jacs.5c17152
J. Am. Chem. Soc. 2026, 148, 4237−4249

result of the electron-withdrawing nature of phosphate groups.[49] The absence of a *P-tg* contribution is not surprising since C6 hydroxymethyl groups of glucose are present mainly in the *gt* and *gg* configurations on the surface of P-CNFs. The *tg* conformer is predominantly found within the cellulose I crystal core, as is expected for native celluloses,[27,31,73] as demonstrated by NMR,[76,77] neutron diffraction,[78] DFT,[77] natural bond orbital[79] and QM/MM[80] analyses. The predominance of the *gt* and *gg* conformations for the C6 groups on the surface of the fibrils was rationalized by gauche stabilization through stereoelectronic $\sigma_{C6-H} \rightarrow \sigma^*_{C5-O5}$ and $\sigma_{C5-H} \rightarrow \sigma^*_{C6-O6}$ interactions.[80]

To estimate the ratio of phosphorylation at the C6 position and its conformational distribution, a ^{13}C multiCP[81] experiment was performed under DNP conditions (Figure 3c). While CPMAS is known not to be quantitative because of very different CP buildup behaviors of carbons depending on their dynamics and the number of nearby protons, the DNP-enhanced multiCP experiment, which employs multiple CP blocks to achieve uniform polarization transfer to ^{13}C, has been shown to provide quantitative intensities with an absolute error of less than 10%.[82] Accurate deconvolution of the C6 peak considering minor species (phosphorylated-C6) requires, however, a very high sensitivity, provided by DNP. In our case, given the width of the CNFs of several nanometers, the DNP enhancement is expected to be uniform over the entire spectrum, which is confirmed by the comparison of the spectra with and without μw irradiation. Moreover, when the integral over the C1 region of the multiCP spectrum is set to 1, integration over the entire carbon spectrum gives a value of 5.95 (Table S1), very close to the theoretical value of 6. On the basis of these results, we assumed that the multiCP experiment remains, in our case, quantitative under DNP conditions. Deconvolution of the C6 resonance was performed considering five contributions, namely, *tg*, *gt*, and *gg* for nonphosphorylated C6 and *P-gt* and *P-gg* for phosphorylated C6. Their respective chemical shifts were set to the values extracted from the 2D INADEQUATE and TEDOR spectra. The line width of each peak of the deconvolution was independently optimized. As a result, the amount of phosphorylated C6 is approximately 16.9%, with a *P-gt*:*P-gg* ratio of 79:21 (Figure 3b, d and Table 1). It should be noted that

Table 1. Estimated Relative Amount of the Different C6 Conformations in P-CNFs from the Deconvolution of the ^{13}C MultiCP Spectrum

Conformation	Ratio (%)
tg	36.5
gt	28.1
gg	18.6
P-gt	13.3
P-gg	3.6

multiple C6 chemical shifts have been reported for cellulose I_β derived from wood,[25] arising from different hydroxymethyl conformations and hydrogen-bonding environments. For curve fitting in this study, only the three dominant conformations (*tg*, *gt* and *gg*) were considered in order to focus on the major phosphorylated species. On the basis of the 18-chain model, where only one-third of the C6 units are exposed on the microfibril surface, this result corresponds to approximately half (50.7%) of the surface C6 units being phosphorylated.

Analysis of the C1−C2 cross peaks from INADEQUATE reveals a dominant C2 resonance at 72.2 ppm and a minor component at 74.8 ppm (Figure 2d-3). The former chemical shift is typical of native cellulose and likely corresponds to nonphosphorylated C2. The latter is assigned to a phosphorylated C2, with a downfield shift (here, ∼2.6 ppm) consistent with phosphorylation. As expected, we also observe a cross peak in the TEDOR spectrum at around 74.8 ppm ^{13}C chemical shift (Figure 2c-1). No evidence of C3 phosphorylation is observed on the INADEQUATE and TEDOR spectra, since this would correspond to a contribution downfield from the native C3 chemical shift at 74.8 ppm (Figure 2d-2). The C5 position can be ruled out because of the absence of hydroxy groups on that carbon.

The amount of phosphorylated C2 sites is difficult to estimate only based on the TEDOR experiment, since the TEDOR cross-peak at 74.8 ppm ^{13}C chemical shift is made of multiple contributions that include through-space polarization transfer from ^{31}P of monophosphate units to P−C2, but also, for instance, C5 adjacent to a P−C6 and C3 adjacent to P−C2 carbons. Nevertheless, assuming an 18-chain model in which one-third of the hydroxyl groups at C2 and C6 positions are exposed on the molecular-chain surface and accessible for modification, the phosphorylation molar ratio of exposed C2 can be determined by matching the total surface charge to the experimental value obtained by potentiometric titration (2.27 mmol g^{-1}), given that the amount of C6 phosphorylation can be determined by the multiCP analysis. It results in approximately one-half of the exposed C6 and one-sixth of the exposed C2 being phosphorylated, meaning that about one-third of the glucose units on the CNF surface carry a phosphate group.

As a result, the interpretation of the DNP INADEQUATE and TEDOR spectra clearly indicates that the phosphate groups are predominantly introduced at the C2 and C6 positions. This finding is in agreement with previous reports on enzymatically hydrolyzed P-CNFs using solution-state NMR.[49] However, in that study, the conformational distribution of the C6 rotamers was lost because of the enzymatic treatment and could not be investigated. In contrast, by working with untreated phosphorylated nanocellulose using DNP-enhanced solid-state NMR, we not only successfully identified the substitution positions but also quantitatively evaluated the different P−C6 conformations. The reduced reactivity of the C3 position is attributed to the intramolecular hydrogen bond formed with the cyclic oxygen atom of the adjacent cellulose monomer unit.[83,84]

To obtain further information about the spatial distribution of the substituents on the CNF surface, a series of DNP-enhanced 2D double-quantum-single quantum (DQ-SQ) $^{31}P-^{31}P$ NMR experiments were performed using the S_3 dipolar recoupling sequence[85−87] with increasing mixing times τ_{mix} (Figure 4 and Figure S3). Owing to DQ coherence filtration, the 2D spectra contain contributions only from coupled ^{31}P spins, i.e., from ^{31}P sites that are sufficiently close in space. Two main correlation peaks can be observed: the expected cross-peaks between the alpha ^{31}P and beta ^{31}P of diphosphate units and, more interestingly, a peak for autocorrelation between monophosphate units. The corresponding dipolar buildup curves were extracted from the 2D data sets and fitted to estimate the average distance (see the Methods section and Figure S4 for details). For the diphosphate units, the buildup can be fitted to a distance of 2.64 Å (Figure S4a−d). Assuming a P−O distance of 1.59 Å, as found in diphosphorus pentoxide,[88] this result leads to an average P−O−P bond angle of 113°. Interestingly, the

https://doi.org/10.1021/jacs.5c17152
J. Am. Chem. Soc. 2026, 148, 4237−4249

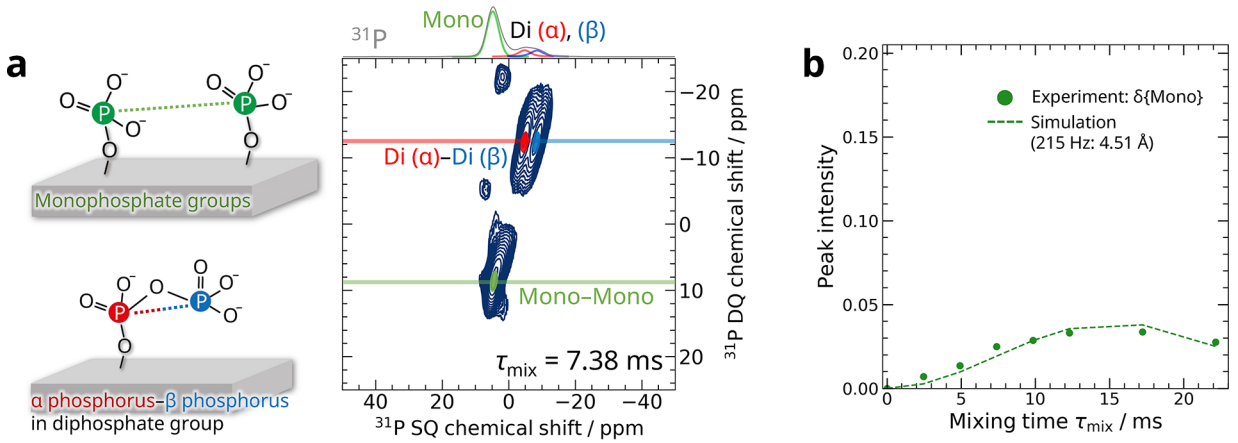

Figure 4. Investigation of the distribution of phosphorus substituents by DNP-enhanced NMR; (a) DNP-enhanced 2D DQ–SQ ^{31}P–^{31}P S_3 spectrum of P-CNFs using a S_3 dipolar recoupling mixing time (τ_{mix}) of 7.38 ms. The assignments and schematics of the different phosphates on the P-CNF structure are given in the figure. (b) Experimental peak intensities of the monophosphate correlation peak from the series of S_3 experiments as a function of τ_{mix}, together with the best fit simulation (dashed line).

buildup of the autocorrelation peak can also be fitted (Figure 4b) using a single distance of 4.51 Å. This suggests that the distribution of the distance between monophosphate units at the P-CNF surface is centered at approximately 4.5 Å.

3.3. Conformational Analysis by MD Simulation

The different experimental findings obtained for the P-CNFs by AFM and DNP-enhanced NMR can now be analyzed by MD simulations. The P-CNF model was constructed on the basis of the 18-chain model of cellulose I_β. More specifically, it contains 18 chains, each with 80 glycosyl residues and ~1.15 mmol g^{-1} monophosphoester groups (total charge: 2.29 mmol g^{-1}), which corresponds to a case where one-half of the surface C6 and one-sixth of the surface C2 are phosphorylated. For simplicity, all phosphate units used in the model are monophosphates. According to the ^{31}P NMR data, the ratio of diphosphate to monophosphate is 1:5.5. The error in the total surface charge is thus expected to be less than 10%.

Details about the model construction are given in the Methods section. This CNF model was equilibrated with an MD production run in water lasting 15 ns. The CNFs twisted in a right-handed manner along the fibril axis, which settled during the production run at a twist angle of 4.2°/nm (see Figure 5a, b), which is in good agreement with the MD-simulated values previously reported for cellulose I-type crystals with ~18 chains.[69,89−91] By calculating the twist period from this twist angle, it would take 86 nm for the CNF to twist 360°, which is close to our AFM results and previously reported AFM observations (~80 nm for highly charged CNFs).[67,69] The phosphorus atom radial distribution function, $g_{P-P}(r)$, calculated from the MD simulation gives the strongest peak at a distance of 5.0 Å (Figure 5d). In our model, this distance corresponds to phosphorus atoms on neighboring glucan chains. This is thus fully consistent with the NMR data, which mostly reveal the shortest distance of ~4.5 Å between phosphate units (Figure 4). Polarization transfer between ^{31}P nuclei from the same cellulosic chain (a distance of ~10 Å in our model) would require a much longer S_3 mixing time, and since ^{31}P nuclei are 100% abundant, they would suffer from dipolar truncation because of the presence of closer phosphorus atoms on neighboring chains.

An overview of the distribution of conformations found by MD simulations for all C6 carbons, regardless of whether they

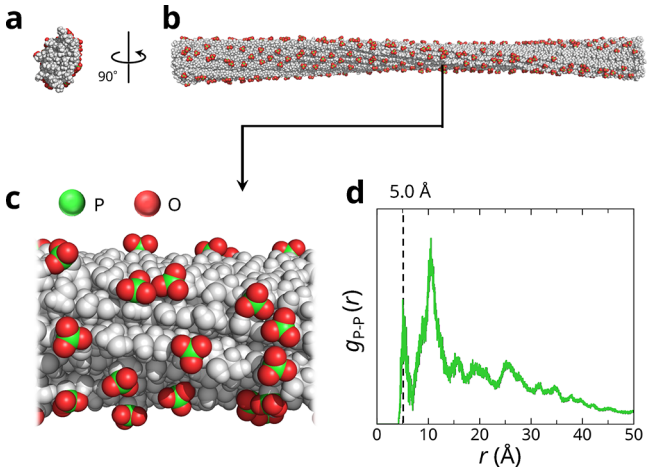

Figure 5. Interphosphorus distances on the surface of P-CNFs from the MD model. (a, b) Snapshot of the equilibrated structure of a P-CNF obtained from a MD simulation in a periodic box filled with TIP3P water lasting 15 ns and (c) enlarged view of the chemical structure at the (1 0 0) surface. Phosphorus, oxygen atoms of the phosphate groups, and all other atoms except protons are colored light green, red and gray, respectively. (d) Radial distribution function between the phosphorus atoms $g_{P-P}(r)$. The function was extracted from the final 1 ns of the trajectories.

are phosphorylated or not, is given in Figure 6a–c. Because cellulose chains have C6 groups pointing on both sides of the chain, alternating between facing one or the other neighboring chain, two conformational distributions are presented for each cellulosic chain in Figure 6a, as discussed by Oehem et al.[92,93] These chains are referred to as the center and origin chains, with the former passing through the center of the monoclinic unit cell of cellulose I and the latter located at the corner of the unit cell. Although these chains are parallel, the center chain is shifted by c/4 along the *c*-axis relative to the origin chain (Figure 6e).[94] Interestingly, for the 6 core molecular chains of the CNFs (i.e., which are not phosphorylated), differences in the preferred C6 conformation are observed between the center and origin chains. Indeed, in the origin chain, the *tg* conformation, derived from cellulose I-type crystals,[57,73] is dominant, whereas in the center chains, the *gg* conformation is preferred. The preference for the *gg* conformation in the center chains can be explained by

https://doi.org/10.1021/jacs.5c17152
J. Am. Chem. Soc. 2026, 148, 4237−4249

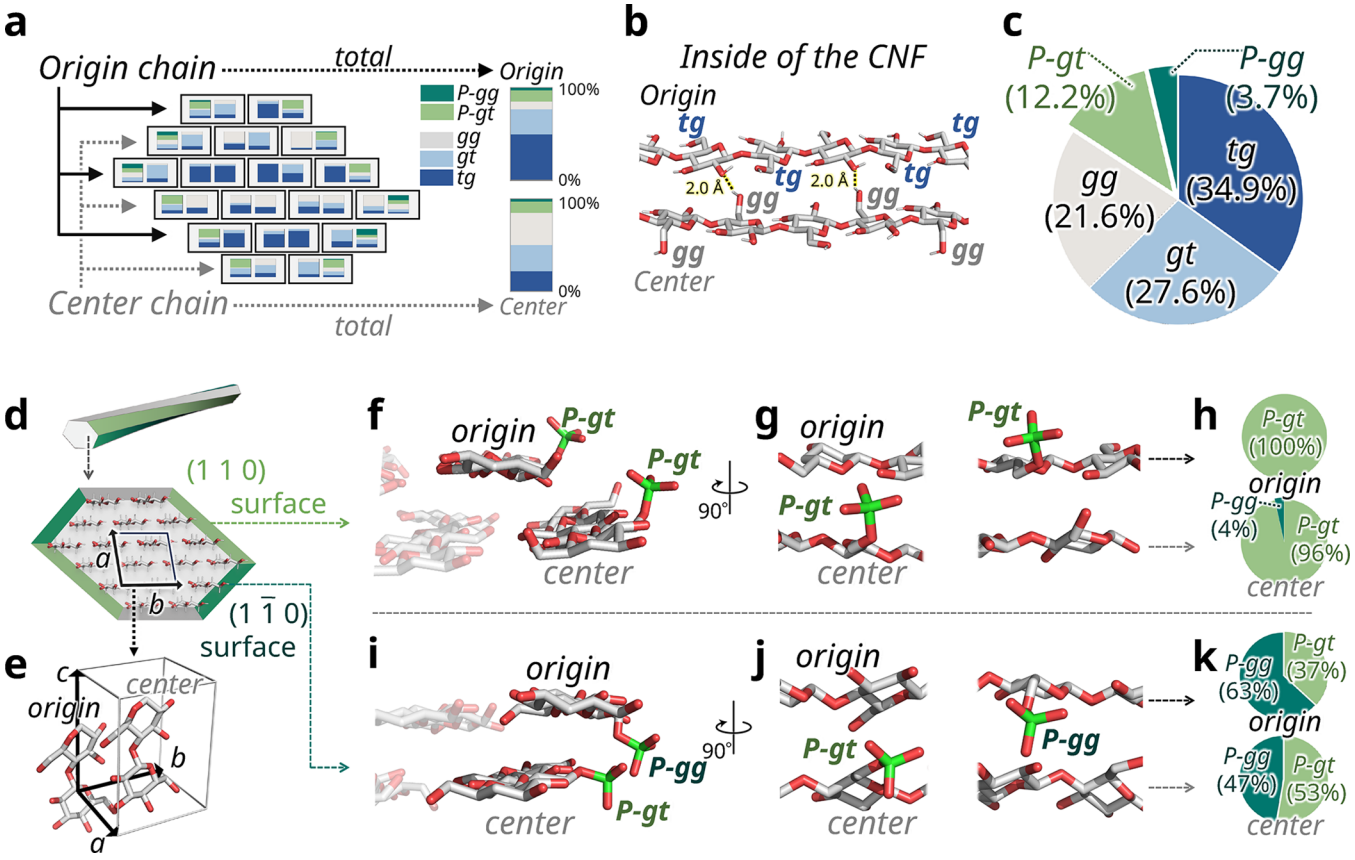

Figure 6. Conformational distribution of P-CNF C6 groups obtained by MD simulation. (a) *tg/gt/gg* conformational distributions of phosphorylated C6 and native C6 in each chain and in total for the center and origin chains in P-CNFs. (b) Representative structure of cellulose molecular chains in the core of P-CNFs. (c) Overall conformational distribution of C6 groups in P-CNFs. (d) Illustration of the P-CNF cross-section and (e) cellulose I_β unit cell. (f–k) Representative conformations of phosphorylated C6 hydroxymethyl groups on the (1 1 0) (f, g) and (1 $\bar{1}$ 0) (i, j) surfaces, together with (h, k) the conformational distribution of phosphorylated C6 groups extracted from the origin and center chains for each surface type. Molecular chains present at the boundary between the (1 1 0) and (1 $\bar{1}$ 0) surfaces are not considered.

the ability of the hydroxymethyl groups, which in that conformation are oriented perpendicular to the plane (Figure 6a and b), to form hydrogen bonds with the C2 hydroxy groups of adjacent origin chains.[92,93,95]

The overall conformational distribution of the C6 groups in the modeled fibril is shown in Figure 6c. Notably, this distribution is in remarkably good agreement with the results of the quantitative multiCP NMR experiment (Table 1), suggesting that the fibril structure modeled by the MD simulations effectively reproduced the overall distribution of C6 conformations experimentally found in P-CNF fibrils by DNP-enhanced NMR. Nevertheless, the proportion of the conformations obtained from MD simulations differs slightly from the experimentally observed proportions. This discrepancy could be explained by the influence of mechanical forces during nanofibrillation, the dispersion in water, and differences in temperature conditions between the MD simulations and the experiments.

Focusing now on the conformation of phosphorylated C6 on the surface chains, interestingly, the phosphate groups on the (1 1 0) surface are predominantly in the *P-gt* conformation (Figure 6f–h). This result can be explained by two factors: a *P-gg* conformation would likely experience steric hindrance with the surface chain below (Figure 6f and g), and the *P-gt* conformer is stabilized not only through stereoelectronic interactions, as discussed above but also by the formation of an intramolecular hydrogen bond (Figure S5a); however, this is not the case for the *P-gg* conformer.

In contrast, the C6 phosphate groups of the origin chains on the (1 $\bar{1}$ 0) surface show a preference for the *gg* conformation (Figure 6i–k). This can primarily be explained by steric hindrance with adjacent chains. Interestingly, a difference in the conformational distribution is observed between the origin and center chains on the (1 $\bar{1}$ 0) surface, with both *gg* and *gt* conformations present in the center chains, with a preference for the *gt* conformation (53%). This is likely due to differences in the ability to form hydrogen bonds, as discussed in detail below on the basis of the results of the DFT calculations. The average ω value of the *gt* conformer is lower on the (1 $\bar{1}$ 0) surface (36.0 ± 14.5° for the center chains and 52.3 ± 8.4° for the origin chains) than on the (1 1 0) surface (61.9 ± 14.5° for the center chains and 58.3 ± 13.1 for the origin chains) (Figure S5b). This can be attributed to greater distortion resulting from steric hindrance with adjacent molecular chains for the *P-gt* conformer on the (1 $\bar{1}$ 0) surface, as shown in Figures 6i and j. Similarly, our MD simulation shows that the phosphoester groups at the C2 position favor conformations that circumvent steric hindrance (Figure S6).

3.4. Rationalizing Phosphorylated C6 Conformations by DFT Calculations

To gain a deeper understanding of the preferred conformations of phosphorylated C6 groups observed both in the NMR

https://doi.org/10.1021/jacs.5c17152
J. Am. Chem. Soc. 2026, 148, 4237–4249

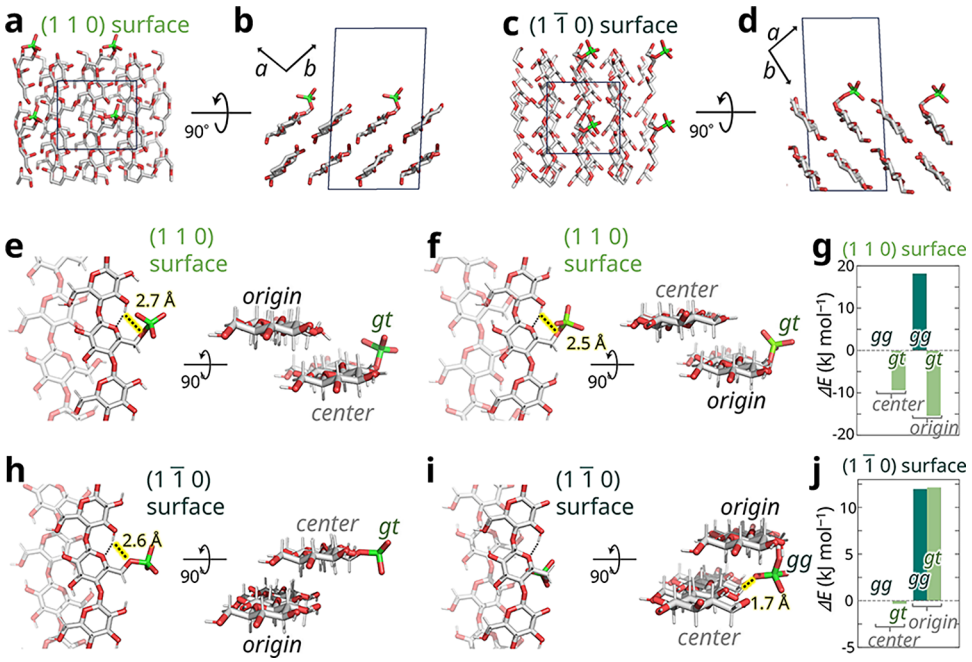

Figure 7. DFT-optimized structures of phosphorylated C6 hydroxymethyl groups. (a, c) Top and (b, d) side views of two-layer slabs for the (1 1 0) and (1 $\bar{1}$ 0) surfaces. Unit cells for the calculations are indicated as parallelograms. (e, f, h, i) Relaxed structures of the outer chains obtained by DFT calculations, with C6 phosphorylation occurring either on the center (e, h) or origin (f, i) chains at the (1 1 0) (e, f) or (1 $\bar{1}$ 0) (h, i) surface. (g, j) DFT-calculated energy difference of the different conformations for each relaxed crystal surface with respect to the energy of the *gg* conformer of the center chains.

experiment and the MD simulation, we conducted DFT calculations to determine the relative energies. To achieve this goal, we constructed slabs consisting of two cellulosic chain layers,[96] as shown in Figures 7a, b and c, d, for the (1 1 0) and (1 $\bar{1}$ 0) P-CNF surfaces. The slabs were created with three-dimensional periodicity under vacuum to construct the crystal surfaces. The structures were then optimized through self-consistent field calculations, and the system energy was subsequently calculated for the relaxed configurations. On the basis of the calculation results, which are consistent with the MD simulations, the *P-gt* conformer was more stable than the *P-gg* conformer on the (1 1 0) surface for both the origin and center chains; the energies of the *P-gt* conformer were 9.4 kJ mol^{-1} and 33.6 kJ mol^{-1} less than those of the *P-gg* conformer for the center and origin chains, respectively (Figure 7g). The stabilization energy can likely be attributed to the ability of the *P-gt* conformation to form O3′-H···O6 and O3′-H···O5 hydrogen bonds (Figure S5a). In contrast, on the (1 $\bar{1}$ 0) surface, the *P-gg* conformer in the origin chains (Figure 7i) has a slightly lower energy than the *P-gt* conformer does (Figure 7j), which is again consistent with the MD simulation results. In addition to avoiding steric interference between the phosphate group and neighboring molecular chain sheets, as observed in the MD model, one of the phosphate oxygens of the *P-gg* conformer can form an intermolecular hydrogen bond with the C2 hydroxy group of adjacent chains (Figure 7i). This interaction contributes to additional stabilization energy. In the center chains, while steric hindrance also provides an energetic advantage to the *P-gg* conformer, it cannot form intra- or intermolecular hydrogen bonds, in contrast to the *P-gt* conformer. As a result, the phosphorylated C6 group in the center chains preferentially adopts the *P-gt* conformer (Figure 7h), which is consistent with the MD results.

Using the energy differences ΔE obtained by DFT, we can now calculate the expected conformer population, p_i, for each crystal surface *i*, assuming a Boltzmann distribution. The results obtained at 105 K and the temperature used for the DNP-enhanced NMR experiments are summarized in Table 2. These populations align perfectly with the conformer distribution at the fibril surfaces derived from the MD simulation (Figure 6a–h).

Table 2. Comparison of the Relative Conformer Populations (%) of Surface Phosphorylated C6 Sites Extracted from MD Simulations or Predicted by DFT Calculations

			Conformation	
Method	Surface	Chain type	*P-gt*/%	*P-gg*/%
MD	(1 1 0)	*origin*	100	0
		center	96.5	3.5
	(1 $\bar{1}$ 0)	*origin*	36.8	63.2
		center	52.6	47.4
DFT	(1 1 0)	*origin*	>99.99	<0.01
		center	>99.99	<0.01
	(1 $\bar{1}$ 0)	*origin*	45.5	54.5
		center	59.2	40.8

In summary, we revealed the atomic-level structure of the nanocellulose surface through experimental DNP-NMR, which was corroborated by computational MD simulations and density functional theory (DFT) calculations. The dramatic improvement in NMR signal intensity achieved by DNP allowed for the quantitative analysis of the regioselectivity of phosphorylation, the distribution of phosphate groups, and their conformation at C6 sites. This information about a single CNF could not have been obtained using TEM, AFM, or conventional solid-state NMR. This hyperpolarization NMR technique has the

https://doi.org/10.1021/jacs.5c17152
J. Am. Chem. Soc. 2026, 148, 4237−4249

advantage of preserving the original crystallinity and morphology of the sample (as with solid-state NMR, but with much higher sensitivity) and is thus applicable not only to P-CNFs but also to any materials, including various types of CNFs—such as surface carboxylated, sulfated, and aminated CNFs—or to other polysaccharides, enabling detailed analysis of their surface chemistry. Therefore, our approach fills a critical gap in understanding the surface structure and material properties of CNFs and can help tailor their properties for specific applications in materials science, biotechnology, and environmental engineering.

■ ASSOCIATED CONTENT

Data Availability Statement

Data supporting the findings of this manuscript are available from the corresponding authors upon reasonable request.

Supporting Information

The Supporting Information is available free of charge at https://pubs.acs.org/doi/10.1021/jacs.5c17152.

AFM images, DNP-enhanced ^{31}P solid-state NMR spectrum, dipolar coupling analysis, MD-simulated conformations of phosphorylated C6 and C2 groups, quantitative ^{13}C multiCP data, and NMR experimental parameters for 1D and 2D experiments. (PDF)

■ AUTHOR INFORMATION

Corresponding Authors

Gaël De Paëpe − *Univ. Grenoble Alpes, CEA, CNRS, IRIG, MEM, 38000 Grenoble, France;* orcid.org/0000-0001-9701-3593; Email: gael.depaepe@cea.fr

Shuji Fujisawa − *Department of Biomaterial Sciences, Graduate School of Agricultural and Life Sciences, The University of Tokyo, 113-8657 Tokyo, Japan;* orcid.org/0000-0002-5221-6781; Email: afujisawa@g.ecc.u-tokyo.ac.jp

Authors

Tomohito Yagita − *Department of Biomaterial Sciences, Graduate School of Agricultural and Life Sciences, The University of Tokyo, 113-8657 Tokyo, Japan; Univ. Grenoble Alpes, CEA, CNRS, IRIG, MEM, 38000 Grenoble, France*

Subhradip Paul − *Univ. Grenoble Alpes, CEA, CNRS, IRIG, MEM, 38000 Grenoble, France*

Wassilios Papawassiliou − *Univ. Grenoble Alpes, CEA, CNRS, IRIG, MEM, 38000 Grenoble, France*

Akane Sakiyama − *Department of Biomaterial Sciences, Graduate School of Agricultural and Life Sciences, The University of Tokyo, 113-8657 Tokyo, Japan;* orcid.org/0009-0006-3507-2655

Yuka Tomita − *Department of Biomaterial Sciences, Graduate School of Agricultural and Life Sciences, The University of Tokyo, 113-8657 Tokyo, Japan;* orcid.org/0009-0002-0051-8179

Tsuguyuki Saito − *Department of Biomaterial Sciences, Graduate School of Agricultural and Life Sciences, The University of Tokyo, 113-8657 Tokyo, Japan;* orcid.org/0000-0003-1073-6663

Sabine Hediger − *Univ. Grenoble Alpes, CEA, CNRS, IRIG, MEM, 38000 Grenoble, France;* orcid.org/0000-0001-5416-8405

Complete contact information is available at: https://pubs.acs.org/10.1021/jacs.5c17152

Notes

The authors declare no competing financial interest.

■ ACKNOWLEDGMENTS

This research was supported by Grants-in-Aid for Young Scientists (grant number 22J21868 to T.Y.) and Grants-in-Aid for Scientific Research (grant numbers JP23K26963, JP23H02270 to S.F., JP21H04733 to T.S.) from the Japan Society for the Promotion of Science (JSPS), JST CREST (grant number JPMJCR22L3 to T.S. and S.F.), and JST ASPIRE (grant number JPMJAP2310 to T.S.) from Japan Science and Technology Agency (JST); the International Exchange Program for Graduate Students and World-leading Innovative Graduate Study Program from the Graduate School of Agricultural and Life Sciences, The University of Tokyo (T.Y.); the French National Research Agency in the framework of the "France 2030" program ANR-17-EURE-0003 through the LabEx Arcane; and the "Investissements d'Avenir" program ANR-15-IDEX-02 through the CDP Glyco@Alps; and the European Research Council Grant ERC-CoG-2015 No. 682895 awarded to G.D.P. The part of this work that was carried out on the Platform for Nanocharacterisation (PFNC) was supported by the "Recherches Technologiques de Base" program of the French National Research Agency (ANR) and the FEDER Program of the Region Auvergne-Rhône-Alpes. We thank the Supercomputer Center, the Institute for Solid State Physics, The University of Tokyo, for the use of their facilities. For the purpose of open access, a CC-BY 4.0 public copyright license has been applied by the authors to the present document and will be applied to all subsequent versions up to the author accepted manuscript arising from this submission (https://creativecommons.org/licences/by/4.0/).

■ REFERENCES

(1) Klemm, D.; Kramer, F.; Moritz, S.; Lindström, T.; Ankerfors, M.; Gray, D.; Dorris, A. Nanocelluloses: A New Family of Nature-Based Materials. *Angew. Chem., Int. Ed.* **2011**, *50* (24), 5438−5466.

(2) Moon, R. J.; Martini, A.; Nairn, J.; Simonsen, J.; Youngblood, J. Cellulose Nanomaterials Review: Structure, Properties and Nanocomposites. *Chem. Soc. Rev.* **2011**, *40* (7), 3941−3994.

(3) Zhu, H.; Luo, W.; Ciesielski, P. N.; Fang, Z.; Zhu, J. Y.; Henriksson, G.; Himmel, M. E.; Hu, L. Wood-Derived Materials for Green Electronics, Biological Devices, and Energy Applications. *Chem. Rev.* **2016**, *116* (16), 9305−9374.

(4) Nechyporchuk, O.; Belgacem, M. N.; Bras, J. Production of Cellulose Nanofibrils: A Review of Recent Advances. *Ind. Crops Prod.* **2016**, *93*, 2−25.

(5) Jakob, H. F.; Fengel, D.; Tschegg, S. E.; Fratzl, P. The Elementary Cellulose Fibril in Picea Abies: Comparison of Transmission Electron Microscopy, Small-Angle X-Ray Scattering, and Wide-Angle X-Ray Scattering Results. *Macromolecules* **1995**, *28* (26), 8782−8787.

(6) Hanley, S. J.; Revol, J. F.; Godbout, L.; Gray, D. G. Atomic Force Microscopy and Transmission Electron Microscopy of Cellulose from Micrasterias Denticulata; Evidence for a Chiral Helical Microfibril Twist. *Cellulose* **1997**, *4* (3), 209−220.

(7) Willhammar, T.; Daicho, K.; Johnstone, D. N.; Kobayashi, K.; Liu, Y.; Midgley, P. A.; Bergström, L.; Saito, T. Local Crystallinity in Twisted Cellulose Nanofibers. *ACS Nano* **2021**, *15* (2), 2730−2737.

(8) Elazzouzi-Hafraoui, S.; Nishiyama, Y.; Putaux, J. L.; Heux, L.; Dubreuil, F.; Rochas, C. The Shape and Size Distribution of Crystalline Nanoparticles Prepared by Acid Hydrolysis of Native Cellulose. *Biomacromolecules* **2008**, *9* (1), 57−65.

(9) Usov, I.; Nyström, G.; Adamcik, J.; Handschin, S.; Schütz, C.; Fall, A.; Bergström, L.; Mezzenga, R. Understanding Nanocellulose Chirality

and Structure-Properties Relationship at the Single Fibril Level. *Nat. Commun.* **2015**, *6*, 7564.
(10) Daicho, K.; Saito, T.; Fujisawa, S.; Isogai, A. The Crystallinity of Nanocellulose: Dispersion-Induced Disordering of the Grain Boundary in Biologically Structured Cellulose. *ACS Appl. Nano Mater.* **2018**, *1* (10), 5774−5785.
(11) Newman, R. H. Estimation of the Lateral Dimensions of Cellulose Crystallites Using 13C NMR Signal Strengths. *Solid State Nucl. Magn. Reson.* **1999**, *15* (1), 21−29.
(12) Kennedy, C. J.; Cameron, G. J.; Šturcová, A.; Apperley, D. C.; Altaner, C.; Wess, T. J.; Jarvis, M. C. Microfibril Diameter in Celery Collenchyma Cellulose: X-Ray Scattering and NMR Evidence. *Cellulose* **2007**, *14* (3), 235−246.
(13) Jakob, H. F.; Fratzl, P.; Tschegg, S. E. Size and Arrangement of Elementary Cellulose Fibrils in Wood Cells: A Small-Angle X-Ray Scattering Study of Picea Abies. *J. Struct. Biol.* **1994**, *113* (1), 13−22.
(14) Rosén, T.; He, H. R.; Wang, R.; Zhan, C.; Chodankar, S.; Fall, A.; Aulin, C.; Larsson, P. T.; Lindström, T.; Hsiao, B. S. Cross-Sections of Nanocellulose from Wood Analyzed by Quantized Polydispersity of Elementary Microfibrils. *ACS Nano* **2020**, *14* (12), 16743−16754.
(15) Paajanen, A.; Zitting, A.; Rautkari, L.; Ketoja, J. A.; Penttilä, P. A. Nanoscale Mechanism of Moisture-Induced Swelling in Wood Microfibril Bundles. *Nano Lett.* **2022**, *22* (13), 5143−5150.
(16) Nixon, B. T.; Mansouri, K.; Singh, A.; Du, J.; Davis, J. K.; Lee, J. G.; Slabaugh, E.; Vandavasi, V. G.; O'Neill, H.; Roberts, E. M.; Roberts, A. W.; Yingling, Y. G.; Haigler, C. H. Comparative Structural and Computational Analysis Supports Eighteen Cellulose Synthases in the Plant Cellulose Synthesis Complex. *Sci. Rep.* **2016**, *6*, No. 28696.
(17) Purushotham, P.; Ho, R.; Zimmer, J. Architecture of a Catalytically Active Homotrimeric Plant Cellulose Synthase Complex. *Science* **2020**, *369* (6507), 1089−1094.
(18) Foster, E. J.; Moon, R. J.; Agarwal, U. P.; Bortner, M. J.; Bras, J.; Camarero-Espinosa, S.; Chan, K. J.; Clift, M. J. D.; Cranston, E. D.; Eichhorn, S. J.; Fox, D. M.; Hamad, W. Y.; Heux, L.; Jean, B.; Korey, M.; Nieh, W.; Ong, K. J.; Reid, M. S.; Renneckar, S.; Roberts, R.; Shatkin, J. A.; Simonsen, J.; Stinson-Bagby, K.; Wanasekara, N.; Youngblood, J. Current Characterization Methods for Cellulose Nanomaterials. *Chem. Soc. Rev.* **2018**, *47* (8), 2609−2679.
(19) Atalla, R. H.; Gast, J. C.; Sindorf, D. W.; Bartuska, V. J.; Maciel, G. E. 13C NMR Spectra of Cellulose Polymorphs. *J. Am. Chem. Soc.* **1980**, *102* (9), 3249−3251.
(20) Earl, W. L.; VanderHart, D. L. High Resolution, Magic Angle Sample Spinning 13C NMR of Solid Cellulose I. *J. Am. Chem. Soc.* **1980**, *102* (9), 3251−3252.
(21) Atalla, R. H.; VanderHart, D. L. Native Cellulose: A Composite of Two Distinct Crystalline Forms. *Science* **1984**, *223* (4633), 283−285.
(22) Horii, F.; Hirai, A.; Kitamaru, R. CP/MAS Carbon-13 NMR Study of Spin Relaxation Phenomena of Cellulose Containing Crystalline and Noncrystalline Components. *J. Carbohydr. Chem.* **1984**, *3* (4), 641−662.
(23) Isogai, A.; Usuda, M.; Kato, T.; Uryu, T.; Atalla, R. H. Solid-State CP/MAS 13C NMR Study of Cellulose Polymorphs. *Macromolecules* **1989**, *22* (7), 3168−3172.
(24) Wang, T.; Hong, M. Solid-State NMR Investigations of Cellulose Structure and Interactions with Matrix Polysaccharides in Plant Primary Cell Walls. *J. Exp. Bot.* **2016**, *67* (2), 503−514.
(25) Wang, T.; Yang, H.; Kubicki, J. D.; Hong, M. Cellulose Structural Polymorphism in Plant Primary Cell Walls Investigated by High-Field 2D Solid-State NMR Spectroscopy and Density Functional Theory Calculations. *Biomacromolecules* **2016**, *17* (6), 2210−2222.
(26) Newman, R. H.; Hemmingson, J. A. Carbon-13 NMR Distinction between Categories of Molecular Order and Disorder in Cellulose. *Cellulose* **1995**, *2* (2), 95−110.
(27) Larsson, P. T.; Wickholm, K.; Iversen, T. A CP/MAS13C NMR Investigation of Molecular Ordering in Celluloses. *Carbohydr. Res.* **1997**, *302* (1−2), 19−25.
(28) Revol, J. F.; Dietrich, A.; Goring, D. A. I. Effect of Mercerization on the Crystallite Size and Crystallinity Index in Cellulose from Different Sources. *Can. J. Chem.* **1987**, *65* (8), 1724−1725.
(29) Yang, H.; Wang, T.; Oehme, D.; Petridis, L.; Hong, M.; Kubicki, J. D. Structural Factors Affecting 13C NMR Chemical Shifts of Cellulose: A Computational Study. *Cellulose* **2018**, *25* (1), 23−36.
(30) Wickholm, K.; Larsson, P. T.; Iversen, T. Assignment of Non-Crystalline Forms in Cellulose I by CP/MAS 13C NMR Spectroscopy. *Carbohydr. Res.* **1998**, *312* (3), 123−129.
(31) Heux, L.; Dinand, E.; Vignon, M. R. Structural Aspects in Ultrathin Cellulose Microfibrils Followed by 13C CP-MAS NMR. *Carbohydr. Polym.* **1999**, *40* (2), 115−124.
(32) Laws, D. D.; Bitter, H.-M. L.; Jerschow, A. Solid-State NMR Spectroscopic Methods in Chemistry. *Angew. Chem., Int. Ed.* **2002**, *41* (17), 3096−3129.
(33) Barnes, A. B.; De Paëpe, G.; van der Wel, P. C. A.; Hu, K.-N.; Joo, C.-G.; Bajaj, V. S.; Mak-Jurkauskas, M. L.; Sirigiri, J. R.; Herzfeld, J.; Temkin, R. J.; Griffin, R. G. High-Field Dynamic Nuclear Polarization for Solid and Solution Biological NMR. *Appl. Magn. Reson.* **2008**, *34* (3−4), 237−263.
(34) Lilly Thankamony, A. S.; Wittmann, J. J.; Kaushik, M.; Corzilius, B. Dynamic Nuclear Polarization for Sensitivity Enhancement in Modern Solid-State NMR. *Prog. Nucl. Magn. Reson. Spectrosc.* **2017**, *102*−*103*, 120−195.
(35) Smith, A. N.; Märker, K.; Hediger, S.; De Paëpe, G. Natural Isotopic Abundance 13C and 15N Multidimensional Solid-State NMR Enabled by Dynamic Nuclear Polarization. *J. Phys. Chem. Lett.* **2019**, *10* (16), 4652−4662.
(36) Hediger, S.; Lee, D.; Mentink-Vigier, F.; De Paëpe, G. MAS-DNP Enhancements: Hyperpolarization, Depolarization, and Absolute Sensitivity. *Handbook of High Field Dynamic Nuclear Polarization*; John Wiley & Sons Ltd: 2020. DOI: 10.1007/s10570-017-1549-6.
(37) Chow, W. Y.; De Paëpe, G.; Hediger, S. Biomolecular and Biological Applications of Solid-State NMR with Dynamic Nuclear Polarization Enhancement. *Chem. Rev.* **2022**, *122* (10), 9795−9847.
(38) Takahashi, H.; Lee, D.; Dubois, L.; Bardet, M.; Hediger, S.; De Paëpe, G. Rapid Natural-Abundance 2D 13C−13C Correlation Spectroscopy Using Dynamic Nuclear Polarization Enhanced Solid-State NMR and Matrix-Free Sample Preparation. *Angew. Chem., Int. Ed.* **2012**, *51* (47), 11766−11769.
(39) Lesage, A.; Lelli, M.; Gajan, D.; Caporini, M. A.; Vitzthum, V.; Miéville, P.; Alauzun, J.; Roussey, A.; Thieuleux, C.; Mehdi, A.; Bodenhausen, G.; Copéret, C.; Emsley, L. Surface Enhanced NMR Spectroscopy by Dynamic Nuclear Polarization. *J. Am. Chem. Soc.* **2010**, *132* (44), 15459−15461.
(40) Kumar, A.; Durand, H.; Zeno, E.; Balsollier, C.; Watbled, B.; Sillard, C.; Fort, S.; Baussanne, I.; Belgacem, N.; Lee, D.; Hediger, S.; Demeunynck, M.; Bras, J.; De Paëpe, G. The Surface Chemistry of a Nanocellulose Drug Carrier Unravelled by MAS-DNP. *Chem. Sci.* **2020**, *11* (15), 3868−3877.
(41) Kang, X.; Kirui, A.; Dickwella Widanage, M. C.; Mentink-Vigier, F.; Cosgrove, D. J.; Wang, T. Lignin-Polysaccharide Interactions in Plant Secondary Cell Walls Revealed by Solid-State NMR. *Nat. Commun.* **2019**, *10*, 347.
(42) Zhao, W.; Kirui, A.; Deligey, F.; Mentink-Vigier, F.; Zhou, Y.; Zhang, B.; Wang, T. Solid-State NMR of Unlabeled Plant Cell Walls: High-Resolution Structural Analysis without Isotopic Enrichment. *Biotechnol. Biofuels* **2021**, *14* (1), 14.
(43) Berruyer, P.; Gericke, M.; Moutzouri, P.; Jakobi, D.; Bardet, M.; Karlson, L.; Schantz, S.; Heinze, T.; Emsley, L. Advanced Characterization of Regioselectively Substituted Methylcellulose Model Compounds by DNP Enhanced Solid-State NMR Spectroscopy. *Carbohydr. Polym.* **2021**, *262*, No. 117944.
(44) Berruyer, P.; Moutzouri, P.; Gericke, M.; Jakobi, D.; Bardet, M.; Heinze, T.; Karlson, L.; Schantz, S.; Emsley, L. Spatial Distribution of Functional Groups in Cellulose Ethers by DNP-Enhanced Solid-State NMR Spectroscopy. *Macromolecules* **2022**, *55* (7), 2952−2958.
(45) Kumar, A.; Watbled, B.; Baussanne, I.; Hediger, S.; Demeunynck, M.; De Paëpe, G. Optimizing Chemistry at the Surface of Prodrug-Loaded Cellulose Nanofibrils with MAS-DNP. *Commun. Chem.* **2023**, *6* (1), 58.

(46) Kang, X.; Kirui, A.; Muszyński, A.; Widanage, M. C. D.; Chen, A.; Azadi, P.; Wang, P.; Mentink-Vigier, F.; Wang, T. Molecular Architecture of Fungal Cell Walls Revealed by Solid-State NMR. *Nat. Commun.* **2018**, *9*, 2747.
(47) Kirui, A.; Ling, Z.; Kang, X.; Dickwella Widanage, M. C.; Mentink-Vigier, F.; French, A. D.; Wang, T. Atomic Resolution of Cotton Cellulose Structure Enabled by Dynamic Nuclear Polarization Solid-State NMR. *Cellulose* **2019**, *26* (1), 329−339.
(48) Kirui, A.; Zhao, W.; Deligey, F.; Yang, H.; Kang, X.; Mentink-Vigier, F.; Wang, T. Carbohydrate-Aromatic Interface and Molecular Architecture of Lignocellulose. *Nat. Commun.* **2022**, *13*, 538.
(49) Zhao, M.; Fujisawa, S.; Saito, T. Distribution and Quantification of Diverse Functional Groups on Phosphorylated Nanocellulose Surfaces. *Biomacromolecules* **2021**, *22* (12), 5214−5222.
(50) Noguchi, Y.; Homma, I.; Matsubara, Y. Complete Nanofibrillation of Cellulose Prepared by Phosphorylation. *Cellulose* **2017**, *24* (3), 1295−1305.
(51) Sauvée, C.; Rosay, M.; Casano, G.; Aussenac, F.; Weber, R. T.; Ouari, O.; Tordo, P. Highly Efficient, Water-Soluble Polarizing Agents for Dynamic Nuclear Polarization at High Frequency. *Angew. Chem., Int. Ed.* **2013**, *52* (41), 10858−10861.
(52) Hoffman, R. Solid-State Chemical-Shift Referencing with Adamantane. *J. Magn. Reson.* **2022**, *340*, No. 107231.
(53) Yesinowski, J. P. High-Resolution NMR Spectroscopy of Solids and Surface-Adsorbed Species in Colloidal Suspension: Phosphorus-31 NMR Spectra of Hydroxyapatite and Diphosphonates. *J. Am. Chem. Soc.* **1981**, *103* (20), 6266−6267.
(54) Helmus, J. J.; Jaroniec, C. P. Nmrglue: An Open Source Python Package for the Analysis of Multidimensional NMR Data. *J. Biomol. NMR* **2013**, *55* (4), 355−367.
(55) Bak, M.; Rasmussen, J. T.; Nielsen, N. C. SIMPSON: A General Simulation Program for Solid-State NMR Spectroscopy. *J. Magn. Reson.* **2000**, *147* (2), 296−330.
(56) Newman, R. H.; Hill, S. J.; Harris, P. J. Wide-Angle x-Ray Scattering and Solid-State Nuclear Magnetic Resonance Data Combined to Test Models for Cellulose Microfibrils in Mung Bean Cell Walls. *Plant Physiol.* **2013**, *163* (4), 1558−1567.
(57) Nishiyama, Y.; Langan, P.; Chanzy, H. Crystal Structure and Hydrogen-Bonding System in Cellulose Iβ from Synchrotron X-Ray and Neutron Fiber Diffraction. *J. Am. Chem. Soc.* **2002**, *124* (31), 9074−9082.
(58) Guvench, O.; Greene, S. N.; Kamath, G.; Brady, J. W.; Venable, R. M.; Pastor, R. W.; Mackerell, A. D. Additive Empirical Force Field for Hexopyranose Monosaccharides. *J. Comput. Chem.* **2008**, *29* (15), 2543−2564.
(59) Guvench, O.; Hatcher, E.; Venable, R. M.; Pastor, R. W.; MacKerell, A. D. CHARMM Additive All-Atom Force Field for Glycosidic Linkages between Hexopyranoses. *J. Chem. Theory Comput.* **2009**, *5* (9), 2353−2370.
(60) Berendsen, H. J. C.; Postma, J. P. M.; Van Gunsteren, W. F.; Dinola, A.; Haak, J. R. Molecular Dynamics with Coupling to an External Bath. *J. Chem. Phys.* **1984**, *81* (8), 3684−3690.
(61) Parrinello, M.; Rahman, A. Polymorphic Transitions in Single Crystals: A New Molecular Dynamics Method. *J. Appl. Phys.* **1981**, *52* (12), 7182−7190.
(62) Giannozzi, P.; Baroni, S.; Bonini, N.; Calandra, M.; Car, R.; Cavazzoni, C.; Ceresoli, D.; Chiarotti, G. L.; Cococcioni, M.; Dabo, I.; Dal Corso, A.; de Gironcoli, S.; Fabris, S.; Fratesi, G.; Gebauer, R.; Gerstmann, U.; Gougoussis, C.; Kokalj, A.; Lazzeri, M.; Martin-Samos, L.; Marzari, N.; Mauri, F.; Mazzarello, R.; Paolini, S.; Pasquarello, A.; Paulatto, L.; Sbraccia, C.; Scandolo, S.; Sclauzero, G.; Seitsonen, A. P.; Smogunov, A.; Umari, P.; Wentzcovitch, R. M. QUANTUM ESPRESSO: A Modular and Open-Source Software Project for Quantum Simulations of Materials. *J. Phys.: Condens. Matter* **2009**, *21* (39), No. 395502.
(63) Grimme, S.; Antony, J.; Ehrlich, S.; Krieg, H. A Consistent and Accurate Ab Initio Parametrization of Density Functional Dispersion Correction (DFT-D) for the 94 Elements H-Pu. *J. Chem. Phys.* **2010**, *132*, No. 154104.
(64) Perdew, J. P.; Burke, K.; Ernzerhof, M. Generalized Gradient Approximation Made Simple. *Phys. Rev. Lett.* **1996**, *77* (18), 3865−3868.
(65) Wada, M.; Sugiyama, J.; Okano, T. The Monoclinic Phase Is Dominant in Wood Cellulose. *Mokuzai Gakkaishi* **1994**, *40*, 50−56.
(66) Ghanadpour, M.; Carosio, F.; Larsson, P. T.; Wågberg, L. Phosphorylated Cellulose Nanofibrils: A Renewable Nanomaterial for the Preparation of Intrinsically Flame-Retardant Materials. *Biomacromolecules* **2015**, *16* (10), 3399−3410.
(67) Arcari, M.; Zuccarella, E.; Axelrod, R.; Adamcik, J.; Sánchez-Ferrer, A.; Mezzenga, R.; Nyström, G. Nanostructural Properties and Twist Periodicity of Cellulose Nanofibrils with Variable Charge Density. *Biomacromolecules* **2019**, *20* (3), 1288−1296.
(68) Khandelwal, M.; Windle, A. Origin of Chiral Interactions in Cellulose Supra-Molecular Microfibrils. *Carbohydr. Polym.* **2014**, *106* (1), 128−131.
(69) Fujisawa, S.; Daicho, K.; Yurtsever, A.; Fukuma, T.; Saito, T. Molecular Dynamics of Drying-Induced Structural Transformations in a Single Nanocellulose. *Small* **2023**, *19* (30), No. 2302276.
(70) Hing, A. W.; Vega, S.; Schaefer, J. Measurement of Heteronuclear Dipolar Coupling by Transferred-Echo Double-Resonance NMR. *J. Magn. Reson. A* **1993**, *103* (2), 151−162.
(71) Zhang, X. C.; Forster, M. C.; Nimerovsky, E.; Movellan, K. T.; Andreas, L. B. Transferred-Rotational-Echo Double Resonance. *J. Phys. Chem. A* **2021**, *125* (3), 754−769.
(72) Lesage, A.; Bardet, M.; Emsley, L. Through-Bond Carbon−Carbon Connectivities in Disordered Solids by NMR. *J. Am. Chem. Soc.* **1999**, *121* (47), 10987−10993.
(73) Horii, F.; Hirai, A.; Kitamaru, R. Solid-State 13C-NMR Study of Conformations of Oligosaccharides and Cellulose - Conformation of CH2OH Group about the Exo-Cyclic C-C Bond. *Polym. Bull.* **1983**, *10* (7−8), 357−361.
(74) Phyo, P.; Wang, T.; Yang, Y.; O'Neill, H.; Hong, M. Direct Determination of Hydroxymethyl Conformations of Plant Cell Wall Cellulose Using 1 H Polarization Transfer Solid-State NMR. *Biomacromolecules* **2018**, *19* (5), 1485−1497.
(75) Yuan, E. C.-Y.; Huang, S.-J.; Huang, H.-C.; Sinkkonen, J.; Oss, A.; Org, M.-L.; Samoson, A.; Tai, H.-C.; Chan, J. C. C. Faster Magic Angle Spinning Reveals Cellulose Conformations in Woods. *Chem. Commun.* **2021**, *57* (34), 4110−4113.
(76) Stenutz, R.; Carmichael, I.; Widmalm, G.; Serianni, A. S. Hydroxymethyl Group Conformation in Saccharides: Structural Dependencies of 2JHH, 3JHH, and 1JCH Spin-Spin Coupling Constants. *J. Org. Chem.* **2002**, *67* (3), 949−958.
(77) Thibaudeau, C.; Stenutz, R.; Hertz, B.; Klepach, T.; Zhao, S.; Wu, Q.; Carmichael, I.; Serianni, A. S. Correlated C-C and C-O Bond Conformations in Saccharide Hydroxymethyl Groups: Parametrization and Application of Redundant 1H- 1H, 13C-1H, and 13C-13C NMR J-Couplings. *J. Am. Chem. Soc.* **2004**, *126* (48), 15668−15685.
(78) Mason, P. E.; Neilson, G. W.; Enderby, J. E.; Saboungi, M. L.; Cuello, G.; Brady, J. W. Neutron Diffraction and Simulation Studies of the Exocyclic Hydroxymethyl Conformation of Glucose. *J. Chem. Phys.* **2006**, *125*, undefined. DOI: 10.1063/1.2393237.
(79) Woodcock, H. L.; Brooks, B. R.; Pastor, R. W. Pathways and Populations: Stereoelectronic Insights into the Exocyclic Torsion of 5-(Hydroxymethyl)Tetrahydropyran. *J. Am. Chem. Soc.* **2008**, *130* (20), 6345−6347.
(80) Barnett, C. B.; Naidoo, K. J. Stereoelectronic and Solvation Effects Determine Hydroxymethyl Conformational Preferences in Monosaccharides. *J. Phys. Chem. B* **2008**, *112* (48), 15450−15459.
(81) Johnson, R. L.; Schmidt-Rohr, K. Quantitative Solid-State 13C NMR with Signal Enhancement by Multiple Cross Polarization. *J. Magn. Reson.* **2014**, *239*, 44−49.
(82) Bertarello, A.; Berruyer, P.; Skantze, U.; Sardana, S.; Sardana, M.; Elmore, C. S.; Schade, M.; Chiarparin, E.; Schantz, S.; Emsley, L. Quantification of Magic Angle Spinning Dynamic Nuclear Polarization NMR Spectra. *J. Magn. Reson.* **2021**, *329*, No. 107030.
(83) Lindh, E. L.; Bergenstråhle-Wohlert, M.; Terenzi, C.; Salmén, L.; Furó, I. Non-Exchanging Hydroxyl Groups on the Surface of Cellulose

Fibrils: The Role of Interaction with Water. *Carbohydr. Res.* **2016**, *434*, 136−142.
(84) Beaumont, M.; Jusner, P.; Gierlinger, N.; King, A. W. T.; Potthast, A.; Rojas, O. J.; Rosenau, T. Unique Reactivity of Nanoporous Cellulosic Materials Mediated by Surface-Confined Water. *Nat. Commun.* **2021**, *12* (1), 1−8.
(85) Teymoori, G.; Pahari, B.; Stevensson, B.; Edén, M. Low-Power Broadband Homonuclear Dipolar Recoupling without Decoupling: Double-Quantum 13C NMR Correlations at Very Fast Magic-Angle Spinning. *Chem. Phys. Lett.* **2012**, *547*, 103−109.
(86) Teymoori, G.; Pahari, B.; Edén, M. Low-Power Broadband Homonuclear Dipolar Recoupling in MAS NMR by Two-Fold Symmetry Pulse Schemes for Magnetization Transfers and Double-Quantum Excitation. *J. Magn. Reson.* **2015**, *261*, 205−220.
(87) Lee, D.; Wolska-Pietkiewicz, M.; Badoni, S.; Grala, A.; Lewiński, J.; De Paëpe, G. Disclosing Interfaces of ZnO Nanocrystals Using Dynamic Nuclear Polarization: Sol-Gel versus Organometallic Approach. *Angew. Chem., Int. Ed.* **2019**, *58* (48), 17163−17168.
(88) Arbib, E. H.; Elouadi, B.; Chaminade, J. P.; Darriet, J. Brief Communication. *J. Solid State Chem.* **1996**, *127* (2), 350−353.
(89) Bu, L.; Himmel, M. E.; Crowley, M. F. The Molecular Origins of Twist in Cellulose I-Beta. *Carbohydr. Polym.* **2015**, *125*, 146−152.
(90) Hadden, J. A.; French, A. D.; Woods, R. J. Unraveling Cellulose Microfibrils: A Twisted Tale. *Biopolymers* **2013**, *99* (10), 746−756.
(91) Kannam, S. K.; Oehme, D. P.; Doblin, M. S.; Gidley, M. J.; Bacic, A.; Downton, M. T. Hydrogen Bonds and Twist in Cellulose Microfibrils. *Carbohydr. Polym.* **2017**, *175*, 433−439.
(92) Oehme, D. P.; Downton, M. T.; Doblin, M. S.; Wagner, J.; Gidley, M. J.; Bacic, A. Unique Aspects of the Structure and Dynamics of Elementary Iβ Cellulose Microfibrils Revealed by Computational Simulations. *Plant Physiol.* **2015**, *168* (1), 3−17.
(93) Oehme, D. P.; Yang, H.; Kubicki, J. D. An Evaluation of the Structures of Cellulose Generated by the CHARMM Force Field: Comparisons to in Planta Cellulose. *Cellulose* **2018**, *25* (7), 3755−3777.
(94) Nishiyama, Y.; Sugiyama, J.; Chanzy, H.; Langan, P. Crystal Structure and Hydrogen Bonding System in Cellulose Iα from Synchrotron X-Ray and Neutron Fiber Diffraction. *J. Am. Chem. Soc.* **2003**, *125* (47), 14300−14306.
(95) Matthews, J. F.; Skopec, C. E.; Mason, P. E.; Zuccato, P.; Torget, R. W.; Sugiyama, J.; Himmel, M. E.; Brady, J. W. Computer Simulation Studies of Microcrystalline Cellulose Iβ. *Carbohydr. Res.* **2006**, *341* (1), 138−152.
(96) Li, Y.; Lin, M.; Davenport, J. W. Ab Initio Studies of Cellulose I: Crystal Structure, Intermolecular Forces, and Interactions with Water. *J. Phys. Chem. C* **2011**, *115* (23), 11533−11539.

https://doi.org/10.1021/jacs.5c17152
J. Am. Chem. Soc. 2026, 148, 4237−4249